Defect-Rich 2D Material Networks for Advanced Oxygen Evolution Catalysts

Bowei Zhang, [†] *Zhiyuan Qi,* [‡#] *Zishan Wu,* [§] *Yu Hui Lui,* [†] *Tae-Hoon Kim,* [#] *Xiaohui Tang,* [†] *Lin Zhou,* [#] *Wenyu Huang,* [‡#] *and Shan Hu** [†]

[†]Department of Mechanical Engineering and [‡]Department of Chemistry, Iowa State University, Ames, Iowa 50011, United States

[#]Ames National Laboratory, U.S. Department of Energy, Ames, Iowa 50011, United States

[§]Department of Chemistry and Energy Sciences Institute, Yale University, New Haven, Connecticut 06511, United States

TOC

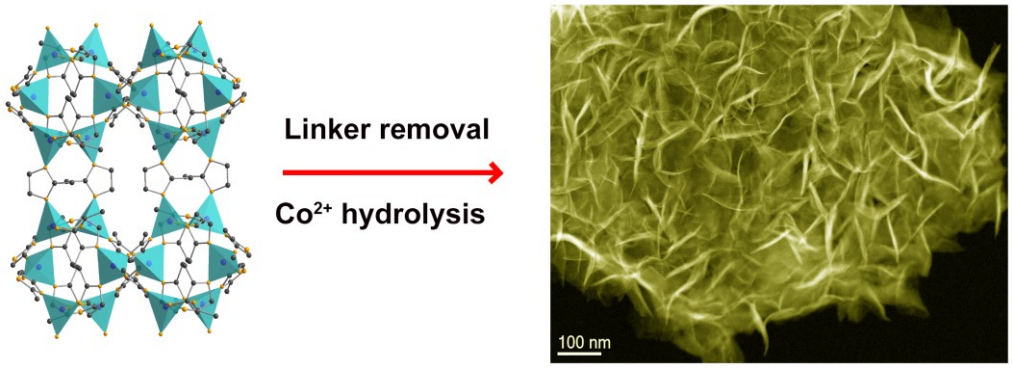

ABSTRACT

A versatile and straightforward room-temperature strategy is demonstrated to synthesize boundary defect-rich ultrathin transition metal hydroxide nanosheet-networks, by *in situ* etching cobalt metal-organic framework (Co-MOF, ZIF-L-Co). The resultant defect-rich ultrathin $Co(OH)_2$ (D-U-$Co(OH)_2$) nanoarrays is one of the most active monometal-based oxygen evolution catalysts up to date. Its activity is 3 ~ 4 times higher than the commercial RuO_2 and superior to the reported exfoliated bimetallic catalysts. Co-MOF can also be grown on various substrates, and the chemical composition of the defect-rich 2D materials is tunable by changing the metal ions in the etchants. Owing to these merits of the unique synthesis route, our work provides an opportunity for synthesizing advanced nanomaterials that are difficult to get access to by conventional methods.

Ultrathin two-dimensional (2D) transition metal hydroxides (TMHs) are attracting an increasing amount of attention as catalysts for electrochemical oxygen evolution reaction (OER) — a sluggish but central reaction to water splitting,[1,2] fuel cells,[3] and metal-air batteries[4] — owing to the higher number of active sites and shorter diffusion length of reactants/products compared to thicker nanosheets.[5,6] These merits grant ultrathin 2D TMHs excellent electrochemical activities, even surpassing the high-cost and scarce benchmark noble metal oxide catalysts. For example, the exfoliated single-layer nanosheets of layered double hydroxides (LDHs, including NiFe, NiCo, and CoCo) reported by Fang *et al.*,[7] showed 40 ~ 54 mV lower overpotentials (η) than the corresponding bulk counterparts at the current density (j) of 10 mA cm^{-2}. Besides, Cui and Wang *et al.* proved that defect engineering is an effective method to increase the number of active sites for electrocatalysis *via* generating massive electrochemically active grain boundaries in transition metal oxides (TMOs).[8,9] After converting TMO nanoparticles into ultra-small nanocrystals with enriched grain boundaries by Li^+ electrochemical tuning (LiET), remarkably higher OER activities can be achieved.[8] Considering the merits of ultrathin morphology and grain boundary (GB) defect, the 2D GB-rich ultrathin TMHs are expected to be efficient electrocatalysts toward OER.

However, incommensurate with the high technical significance, the synthesis of ultrathin 2D TMHs is currently limited mainly to exfoliation and hydrothermal methods.[5,7,10–13] Exfoliation method is hazardous and requires complex procedures with low yields. Moreover, the exfoliated single-layer nanosheets are prone to re-stack during the required post-casting procedure. The hydrothermal process generally involves harsh conditions and lack of control over the thickness of nanosheets. Moreover, the massive boundaries are normally produced by the complex LiET method.[8,9,14] Despite the grain boundary-rich ultrathin TMHs could be obtained by applying

LiET to exfoliated or hydrothermally-grown nanosheets, this synthetic route is unfeasible for large scale production. It is therefore of great significance to develop more efficient, simpler, and safer methods for scalable synthesis of GB-rich ultrathin 2D TMHs.

Metal-organic frameworks (MOFs) are composed of metal nodes and organic linkers and have abundant atomically dispersed metal sites.[15] However, few of them are used for electrocatalysis because of their poor electrical conductivity.[16,17] The widely reported strategies to render MOF conductive, like pyrolysis and hybridization with secondary conductive supports, often sacrifice MOF's molecular active sites.[16,18] Considering the atomically dispersed metal atoms and the abundant pores in MOFs, the linkers can be homogeneously removed by an *in situ* etching process, leaving the metal parts to coordinate with OH^- in the solution to achieve ultrathin TMHs.[19] As the etching process occurs homogeneously through the whole MOFs, the nucleation sites form through the whole structure and the TMHs grow along different orientations. This homogenous growth process should be different from the oriented bottom-up growth processes.[20]

We, therefore, hypothesize that without applying elevated temperature and pressure, as in the case of hydrothermal growth, the etching process will produce TMHs with a low degree of crystallinity and abundant GB defects, which will improve their OER activity. Herein, we developed a room-temperature strategy to fabricate hierarchically structured boundary-rich ultrathin Co-based hydroxide nanosheets on 3D conductive nickel foam. As shown in Scheme 1, the well-aligned cobalt MOF (ZIF-L-Co) nanosheets were initially grown on Ni foams and then following by *in situ* etching treatment. The resulting defect-rich ultrathin $Co(OH)_2$ (D-U-$Co(OH)_2$) showed an attractive electrocatalytic activity toward OER in alkaline electrolyte. Besides monometallic TMHs, bimetallic nano-polycrystalline CoNi hydroxides can be obtained by the similar synthetic route, which demonstrates the general applicability of this room-

temperature strategy for synthesizing advanced nanomaterials for energy storage and conversion applications.

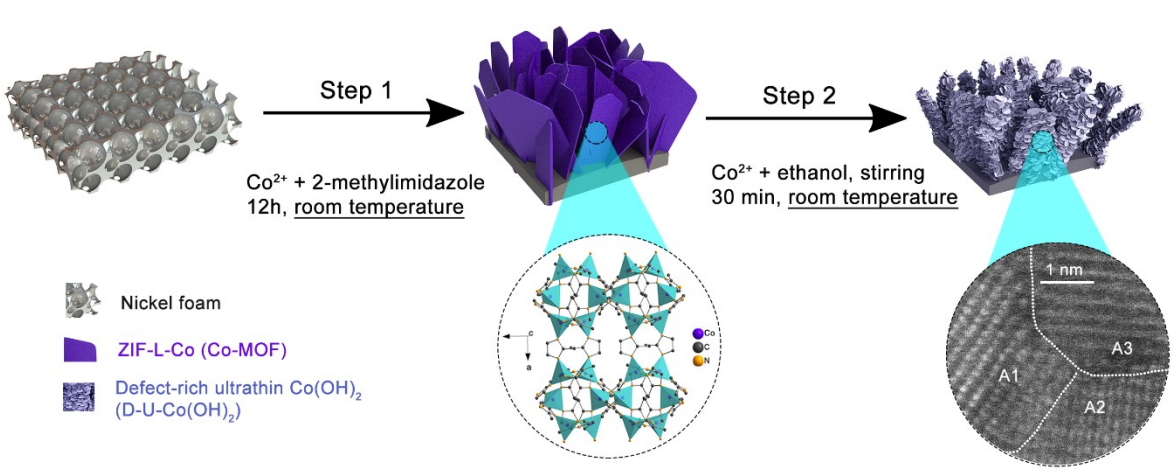

Scheme 1. The synthetic route for Co-MOF nanoarrays and defect-rich ultrathin $Co(OH)_2$ nanosheet-networks on 3D Ni foam.

We first studied the synthesis of mono-metallic $Co(OH)_2$ nanosheets and investigated the effects of ultrathin morphology and boundary defect on its electrocatalytic activity. As depicted in Scheme 1, a room-temperature, solution phase method was used to synthesize well-aligned Co-MOF nanosheets supported on three-dimensional (3D) conductive Ni foam. The obtained Co-MOFs were subsequently converted into defect-rich ultrathin cobalt hydroxide (denoted as D-U-$Co(OH)_2$) by an *in situ* etching process using cobalt ethanolic solution (see details from the experimental section). The photographs of bare Ni foam, Co-MOF, and D-U-$Co(OH)_2$ electrodes are presented in Figure S1. The purple and light blue colors are consistent with that of Co- MOF and cobalt hydroxide, respectively.

The Co-MOF nanoarrays were initially characterized by field-emission scanning electron microscopy (FESEM) and X-ray diffraction (XRD). FESEM images in Figure 1a and S2 reveal the smooth Co-MOF nanosheets array grown on Ni foams. The crystal structure and crystallinity of as-synthesized Co-MOF were confirmed by XRD. The resultant XRD patterns (Figure S3) match with that of the reported ZIF-L-Co (orthorhombic, space group *Cmce*), which has two-dimensional layered structures.[21] The experimental result shows a slight right shift compared to the simulated pattern, which could result from about 2% lattice compression in all dimensions. Energy-dispersive X-ray (EDX) spectroscopy mapping in Figure S4 demonstrates the homogeneous distribution of Co, C, and N elements through Co-MOF without O and Ni elements in it. Interestingly, the purple MOF layer is not readily formed on the Ni foam in the first 6 hours (Figure S5a). However, when the bare Ni foam was first immersed into 2-methylimidazole aqueous solution overnight, a uniform purple layer can be observed on Ni foam in 6 hours (Figure S5b). The growth mechanism of Co-MOF in the precursor solution (Co^{2+} and 2-methylimidazole) (step 1 in Scheme 1) is therefore believed as following: 2-methylimidazole molecules are initially adsorbed on the Ni foam surface and then coordinate with Co^{2+} ions in the aqueous solution to form ZIF-L-Co.

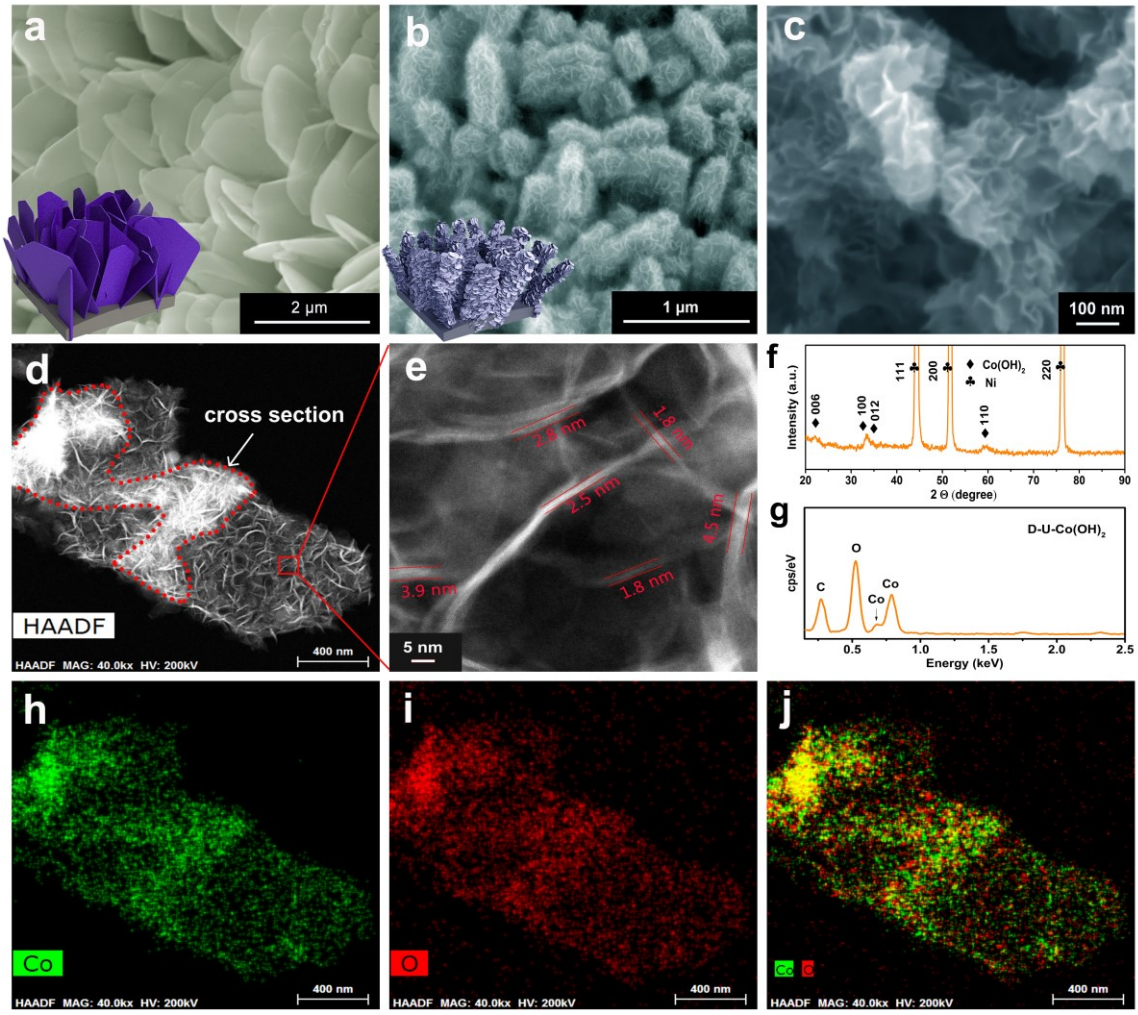

Figure 1. Characterizations of Co-MOF and MOF-derived ultrathin $Co(OH)_2$. FESEM images of (a) Co-MOF nanoarrays and (b, c) MOF-derived ultrathin $Co(OH)_2$. (d, e) HAADF-STEM images, (f) XRD, (g) EDX spectra, and (h-j) mapping of MOF-derived ultrathin $Co(OH)_2$.

After the *in situ* etching in the ethanol solution of cobalt chloride hexahydrate (pH = 6 ~ 7) for 30 min at room-temperature, the nanosheet morphology of Co-MOF was partly inherited while the nanosheets surface became rough (Figure S6 and 1b). As shown in Figure 1a, 1b, and S6, the lateral size of the MOF-derived nanosheets decreased significantly compared to the parent MOFs.

These structural changes might be originated from the removal of organic linkers and structural reconstruction during the etching process. The zoom-in FESEM image of MOF-derived rough nanosheets (Figure 1c) shows a layer of smaller and ultrathin nanosheet arrays on the surface of bigger nanosheets underneath. The high-angle-annular-dark-field scanning transmission electron microscopy (HAADF-STEM) was then used to precisely characterize the morphology of those unique structures. The side and cross-section views are shown in Figure 1d and e. The HAADF-STEM images clearly reveal that MOF-derived nanosheets are constructed by hierarchically interconnected ultrathin nanosheets. The thickness of these ultrathin nanosheets was less than 5 nm estimated from the zoom-in HAADF-STEM image (Figure 1e). It is necessary to note that some thicker parts in Figure 1d and 1e could be due to the tilt or the curly edge of the ultrathin nanosheets, which do not represent the real thickness of the nanosheets (see details in Figure S7). Atomic Force Microscopy (AFM) was used to characterize the ultrathin nanosheets as well. As the space between ultrathin nanosheets is too small compared to the AFM tip, it is inappropriate to directly scan the substrate surface with ultrathin nanosheet layer. We then peeled the ultrathin nanosheets by sonication for the AFM characterization. As shown in Figure S8, the AFM height profiles indicate that the thickness of the nanosheets is 2 ~ 5 nm. This thickness is consistent with the thickness value that is estimated from the HR-HAADF-STEM images.

XRD pattern in Figure 1f shows the MOF-derived nanosheets have no diffraction peaks from the original Co-MOF but a new set of diffraction peaks well indexed to (006), (100), (012), and (111) facets of $Co(OH)_2$ (PDF# 00-002-0925), indicating the nanosheets are composed of $Co(OH)_2$. EDX spectra (Figure 1g) and elemental mapping (Figure 1h-i) demonstrate the MOF-derived nanosheets are only dominated by Co and O elements, and the disappearance of N element (~ 0.4 keV) suggests the removal of organic linkers. Besides, a strong N peak was

observed in the EDX spectra of the sample etched for 10 min, due to the incomplete conversion from Co-MOFs into inorganic $Co(OH)_2$ (Figure S9). With all the above characterizations, we can safely conclude that the Co-MOFs were fully converted into hierarchically structured ultrathin 2D $Co(OH)_2$ nanosheet networks after 30 min etching. We used 100 mL of 0.025 M $CoCl_2.6H_2O$ ethanol solution as etchant. The excessive amount of ethanol in the etchant can replace the H_2O coordinated with cobalt ions and release it. With the released water, there is a hydrolysis equilibrium ($Co^{2+} + 2H_2O \leftrightarrow Co(OH)_2 + 2H^+$). This hydrolysis reaction has been reported in aqueous/ethanolic solutions of different cobalt salts and has previously been used to synthesize CoO_xH_y.[22,23] The slight acidity of as-synthesized Co ethanolic etchant solution (pH: 5 ~ 6) was confirmed by pH meter and pH paper, showing that the hydrolysis equilibrium does occur in the etchant solution. When Co-MOF on nickel form is inserted into the etchant, the H^+ produced from the aforementioned hydrolysis etches the MOF and release Co^{2+} ($Co(N-N)_2 + 2H^+ \leftrightarrow Co^{2+} + 2(N-NH)$), both of which can move the hydrolysis equilibrium to the right and prompt the Co^{2+} hydrolysis (see details in Supporting Information). After Co-MOF has been inserted into the etchant for 30min, the final pH of etchant was measured to be ~7.0, as compared to the pH of 5~6 for the as-prepared etchant. When 5.92×10^{-15} was used as the solubility product constant (Ksp) of $Co(OH)_2$, the equilibrium pH was calculated as 7.3, which is very close to the measured value of ~7.0, therefore we believe $Co(OH)_2$ exists in the final etchant solution and that the D-U-$Co(OH)_2$ is formed via the proposed hydrolysis-controlled MOF-etching process. The ultrathin feature of the $Co(OH)_2$ nanosheets is the result of the thorough etching process made possibly by MOFs' porous structures that are easily accessible to the etching solution.

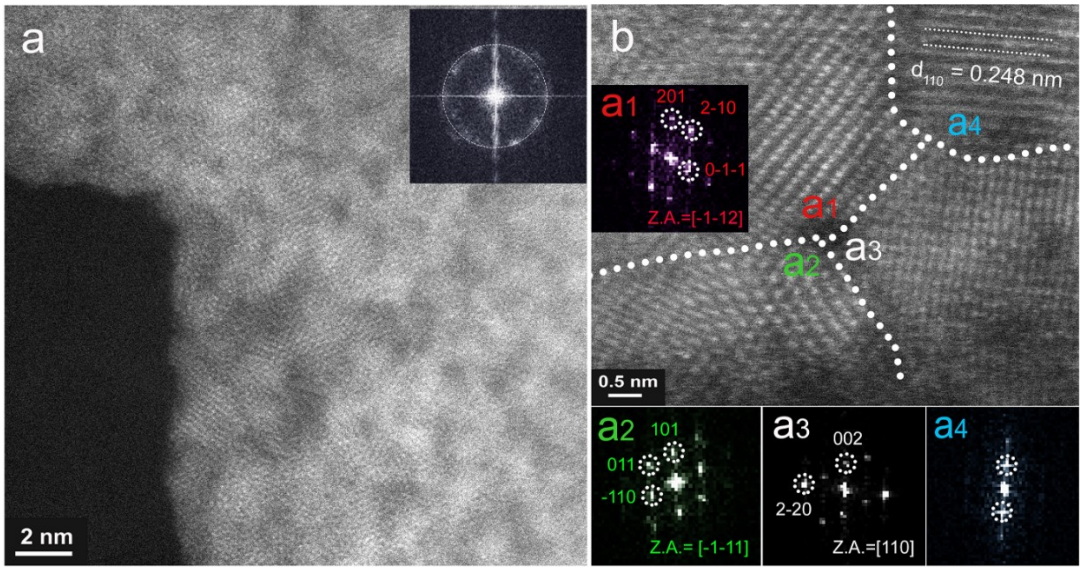

Figure 2. (a) HAADF-STEM images of MOF-derived D-U-$Co(OH)_2$. (b) High-resolution HAADF-STEM image of nano-grains and boundary defects in D-U-$Co(OH)_2$. Inserted images are the corresponding fast Fourier Transformation (FFT) images.

High-resolution HAADF-STEM was then employed to investigate the crystal grains of D-U-$Co(OH)_2$. As shown in Figure 2, the ultrathin nanosheet is nano-polycrystalline with in-plane randomly oriented nano-sized grains. The fast Fourier Transformation (FFT) image inserted in Figure 2a shows a typical circle pattern of nano-polycrystalline even if the scale bar is only 2 nm.[8] FFT patterns in Figure 2b demonstrate that different grain areas (from a_1 to a_4) have different orientations and can be well indexed to the crystal planes of $Co(OH)_2$ (Detailed crystal indexing information in Table S1). HAADF-STEM image in Figure S10 further confirms the nano-polycrystalline nature and reveals the grain size is less than 5 nm. Due to these small nano-sized grains (< 5 nm) and thus the high density of boundaries, D-U-$Co(OH)_2$ exposes a large amount of active sites on the surface for electrocatalysis reactions.[8,9,14]

A thicker $Co(OH)_2$ nanosheets layer on Ni foam was synthesized as control sample by immersing the obtained Co-MOF@Ni foam into 1M KOH electrolyte (pH ~ 13.6) at room temperature with stirring. As Co-MOF is unstable in strong alkaline media, it was rapidly (within a few minutes) converted into $Co(OH)_2$ nanosheets with the thickness from 60 nm ~ 200 nm (Figure S11-13). In this work, the thick $Co(OH)_2$ is denoted as T-$Co(OH)_2$ (mass loading ~ 2.7 ± 0.37 mg cm^{-2}). The XRD pattern of T-$Co(OH)_2$ (Figure S12) shows much sharp and stronger peaks than those of D-U-$Co(OH)_2$, indicating the T-$Co(OH)_2$ has a higher crystalline degree, as also confirmed by TEM images (Figure S13). These results suggest that the rapid decomposition of Co-MOF in strong alkaline condition tend to produce thicker $Co(OH)_2$ with a higher crystalline degree.

The sensitive X-ray photoelectron spectroscopy (XPS) was further carried out to analyze the surface chemical composition of D-U-$Co(OH)_2$. As shown in Figure S14a, XPS survey spectra demonstrate the coexistence of Co and O without N, which agrees well with the mapping result. The Co $2p_{3/2}$ spectra (Figure S14b) was fitted into two peaks with the main Co^{2+} peak at 780.1 eV and a shakeup satellite at 788.7 eV.[24,25] The O 1s peaks at 531.0 eV and 529.1 eV (Figure S14c) can be indexed to metal hydroxides and lattice oxygen, respectively.[25]

The activity of D-U-$Co(OH)_2$ catalyst toward OER was assessed in argon-saturated 1M KOH by using polarization curve at a scan rate of 5 mV s^{-1}. Figure 3a shows the overpotential of D-U-$Co(OH)_2$ required to reach j = 10 mA cm^{-2}_{geo} (current normalized to the geometric area of the electrode) is as low as 236 mV before iR-correction (where i and R represent the current and ohmic resistance, respectively) and even lower at 223 mV after applying a 90% iR-correction. Besides, the estimated onset potential of D-U-$Co(OH)_2$ (~ 1.39 V) is 80 mV lower than that of T-$Co(OH)_2$ (~ 1.47 V). As onset potential is an important factor to judge the intrinsic activity of

catalyst,[26] the significantly reduced onset potential of D-U-$Co(OH)_2$ reveals its higher intrinsic activity than T-$Co(OH)_2$. At η = 300 mV, the current density of D-U-$Co(OH)_2$ is as high as 30.8 mA cm^{-2} which is 2.5 ~ 3 times larger than T-$Co(OH)_2$ and commercial RuO_2 (Figure 3b), showing the superior activity toward OER. The catalyst's excellent stability was then demonstrated by chronopotentiometry holding at 20 mA cm^{-2} for 20 hours and no significant potential fluctuation was observed in Figure 3c. After the long-time stability test, the post-OER D-U-$Co(OH)_2$ maintained the nanosheet morphology and nano-polycrystalline nature, as demonstrated by FESEM/STEM images and the circle-like FFT pattern (Figure S15). Therefore, D-U-$Co(OH)_2$ has a good stability for OER under alkaline condition. We then compared the overpotential of D-U-$Co(OH)_2$ at 10 mA cm^{-2} with the reported state-of-the-art Co-based catalysts, as shown in Figure 3d (see details in Table S2). D-U-$Co(OH)_2$ has much lower overpotential than the mono-metallic Co oxide/hydroxides-based catalysts and is even comparable to the state-of-the-art Ni/Fe-based multi-metallic compounds. The catalytic kinetics of D-U-$Co(OH)_2$ and T-$Co(OH)_2$ for OER were examined by Tafel plot, and the two samples show similar Tafel slopes as 131 mV dec^{-1} (Figure S16). Notably, the mass loading of T-$Co(OH)_2$ (~ 2.7 mg cm^{-2}) is 3.9 times of D-U-$Co(OH)_2$ (~ 0.62 mg cm^{-2}), which reflects the superior activity and efficiency of D-U-$Co(OH)_2$ as the Tafel slope is usually influenced by catalyst mass loading.

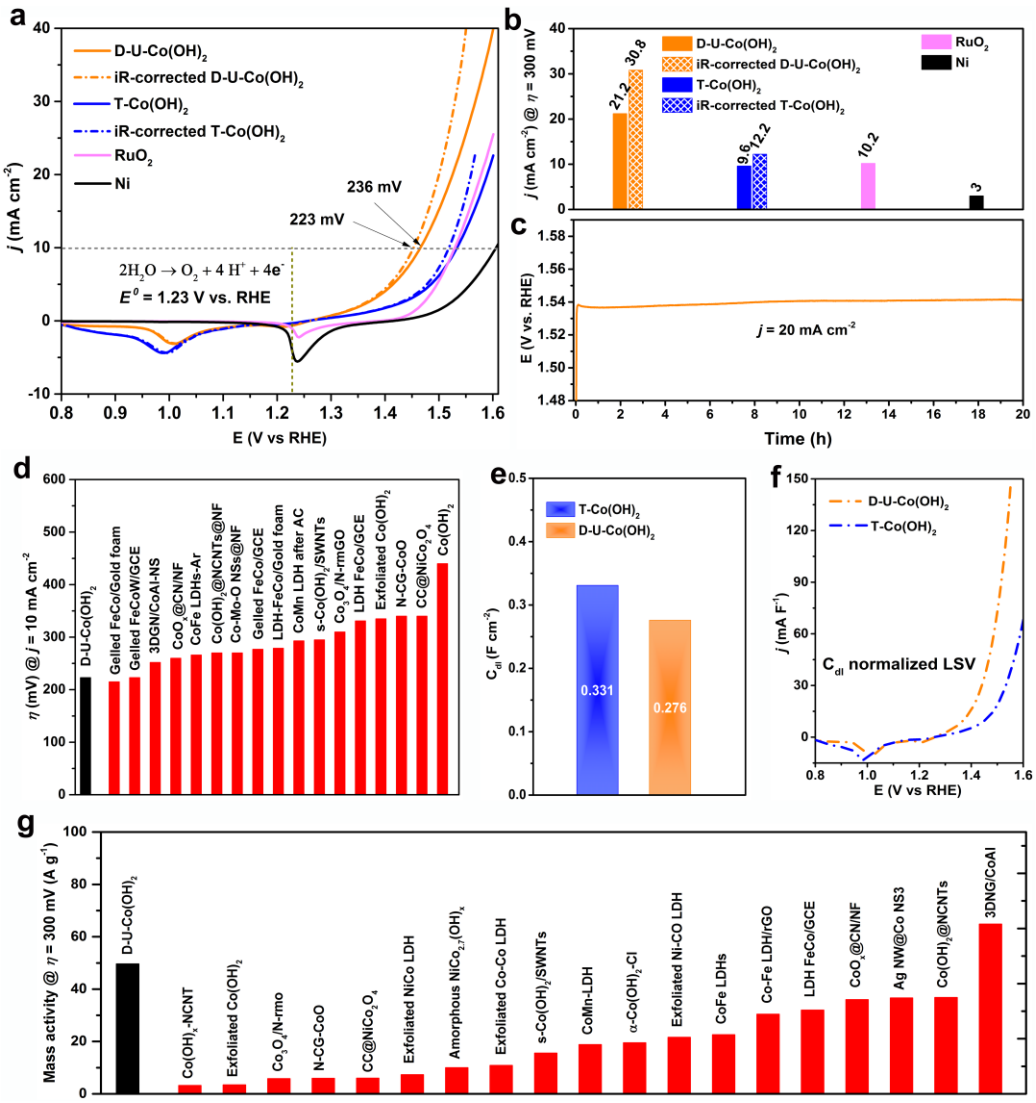

Figure 3. (a) OER polarization curves and (b) the current densities at η = 300 mV of D-U-Co(OH)$_2$, T-Co(OH)$_2$, commercial RuO$_2$, and bare Ni foam in 1M KOH. (c) Stability test of D-U-Co(OH)$_2$. (d) Comparison of η @ j = 10 mA cm^{-2}. (e) C_{dl} and (f) the C_{dl}-normalized polarization curves. (g) Comparison of mass activity @ η = 300 mV. References cited in panels (d) and (g): Gelled FeCo/Gold foam,[27] Gelled FeCoW/GCE,[27] 3DGN/CoAl-NS,[28] Co$_x$@CN/NF,[29] CoFe-LDHs-Ar,[30] Co(OH)$_2$@NCNTs@NF,[31] Co-Mo-O NSs@NF,[32] Gelled FeCo/GCE,[27] LDH-FeCo/Gold foam,[27] CoMn LDH after AC,[33] s-Co(OH)$_2$/SWNTs,[34] Co$_3$O$_4$/N-rmGO,[35] LDH FeCo/GCE,[27] Exfoliated Co(OH)$_2$,[34] N-CG-CoO,[36] CC@NiCo$_2$O$_4$,[36] Co(OH)$_2$,[37]

$Co(OH)_x$-NCNT,[38] Exfoliated NiCo LDH,[13] Armorphous $NiCo_{2.7}(OH)_x$,[39] Exfoliated Co-Co LDH,[7] CoMn-LDH,[33] α-$Co(OH)_2$-Cl,[40] Exfoliated Ni-Co LDH,[7] CoFe LDHs,[30] CoFe LDH/rGO,[41] Ag NW@Co NS3.[42]

The active surface area is one of the vital factors that are responsible for the activity of catalysts, and the double layer capacitance (C_{dl}) is believed to reflect the electrochemical surface area (ECSA).[26,27,43] As the oxyhydroxide will become conductive at or above the OER onset potential, we therefore measured the C_{dl} values of D-U-$Co(OH)_2$ and T-$Co(OH)_2$ using electrochemical impedance spectroscopy (EIS) at DC bias of 1.55 V vs RHE (see details in Figure S17).[44] Based on the EIS results, the mass-normalized C_{dl} of D-U-$Co(OH)_2$ (0.45 F g^{-1}) is ~ 4.5 times of T-$Co(OH)_2$ (0.10 F g^{-1}), indicating the D-U-$Co(OH)_2$ has larger amount of active sites/unit mass. As shown in Figure 3f, the polarization plots of D-U-$Co(OH)_2$ and T-$Co(OH)_2$ were normalized by their corresponding C_{dl} values. The intrinsic activity of D-U-$Co(OH)_2$ is much higher than that of T-$Co(OH)_2$. Thus, the high electrocatalytic activity of D-U-$Co(OH)_2$ is mainly originated from its high intrinsic activity, as confirmed by the significantly reduced onset potential.[45–47] As the changes in crystallinity, structural size, etc. can significantly alter the intrinsic activity of catalysts,[26,48] the higher intrinsic activity of D-U-$Co(OH)_2$ than T-$Co(OH)_2$ could be ascribed to the ultrathin and defective natures. To better evaluate the catalytic activity of the D-U-$Co(OH)_2$, we calculated its mass activity at η = 300 mV by using total catalyst mass and compared it with the reported Co-based OER catalysts.[43,49,50] As shown in Figure 3g, the mass activity of D-U-$Co(OH)_2$ is at least an order of magnitude higher than the CoH_xO_y-based mono-metal catalysts, much higher than the exfoliated Co-M (M = Co, Ni, Fe, Mn, Zn) layered double hydroxides

(LDHs), and comparable to the bimetallic Co-based compounds that have massive cation/anion vacancy defects (detail comparison is listed in Table S3).

However, Boettcher *et al*. reported that the sub-ppm levels of Fe impurity in the as-synthesized KOH electrolyte could be incorporated into NiOOH.[51] In order to investigate whether or not the impressive OER activity is contributed by Fe incorporation,[52] we conducted OER activity measurements of D-U-$Co(OH)_2$ in both purified 1M KOH and 2 mM Fe + unpurified 1M KOH electrolytes, without applying iR-correction. The sub-ppm level Fe impurity in the unpurified 1M KOH was removed by hydrothermally synthesized cobalt hydroxide powder (see details from the experimental section). The electrolyte used through this work is unpurified 1M KOH solution unless otherwise noted. As shown in Figure S18a, the OER activity of D-U-$Co(OH)_2$ in purified 1M KOH electrolyte is slightly lower than that in the unpurified electrolyte. In the 2 mM Fe + unpurified 1M KOH electrolyte, the OER activity is significantly increased. These results agreed with previous studies that the Fe impurity in the electrolyte could affect the OER activity of the electrocatalyst. However, in our study the Fe impurity affects the observed OER activity of D-U-$Co(OH)_2$ only to a limited extent, possibly due to the low concentration of Fe in the unpurified 1M KOH electrolyte. Considering most of the OER activities reported in literatures were tested in unpurified KOH electrolyte, we kept the OER results obtained in the as-prepared 1M KOH electrolyte for comparison with the previously reported OER catalysts. In order to further demonstrate the superiority of our synthesis method, we deposited the CoO_xH_y on Ni foam by electrodeposition method with a mass loading of 0.6 ~ 0.7 mg cm^{-2}, similar to the 0.62 mg cm^{-2} mass loading of D-U-$Co(OH)_2$, and compared its OER activity with that of D-U-$Co(OH)_2$ in the purified 1M KOH electrolyte. In Figure S18b, the D-U-$Co(OH)_2$ shows a significant higher OER

activity than that of the electrodeposited CoO_xH_y. The inset SEM image in Figure S18b shows the morphology of electrodeposited CoO_xH_y on Ni foam.

Nickel (Ni) is another extensively investigated element for OER and the incorporation of Ni into Co hydroxide can significantly improve the OER activity due to the synergetic effect.[7,53] To preliminarily test the general applicability of the room-temperature synthesis route, we replaced the $\{Co^{2+}$ + ethanol$\}$ etchant by $\{Ni^{2+}$ + ethanol$\}$ to etch the Co-MOF and obtained ultrathin defect-rich CoNi hydroxide (D-U-CoNi-OH, 0.27 mg cm^{-2}). As shown in Figure 4a and b, the D-U-CoNi-OH uniformly grow on Ni foam but its morphology is different from D-U-$Co(OH)_2$. The similar ultrathin and defect-rich nature of D-U-CoNi-OH are demonstrated by the HAADF-STEM images (Figure 4c and f), TEM images and corresponding FFT patterns (Figure 4d and Figure S19), SAED pattern (Figure 4e), and the EDX elemental mapping (Figure 4g-j). It is nano-polycrystalline with a thickness of 3 ~ 4 nm.[8,54] The EDX spectra in Figure S20 indicates the atomic ratio of Co: Ni is 48.9: 51.1, which is close to the reported optimal ratio.[55] Its electrocatalytic activity toward OER was tested under the same condition as mentioned above. As expected, the D-U-CoNi-OH only needed 228 mV overpotential to deliver a 10 mA cm^{-2} current density (Figure S21) with a small Tafel slope of 57 mV dec^{-1} after a 90% iR-correction (Figure S22) in unpurified 1M KOH. Despite the mass loading of D-U-CoNi-OH is only about 43% of D-U-$Co(OH)_2$, its kinetics (reflected by Tafel slope) and the activity at high voltage are much higher than D-U-$Co(OH)_2$ (see details from Table S2 and 3). At η = 300 mV, the current density of D-U-CoNi-OH reaches as high as 89.9 mA cm^{-2}, and its turnover frequency (0.092 s^{-1}) and mass activity (332.96 A g^{-1}) are even favorably comparable to the reported state-of-the-art Ni/Fe-based catalysts (see details in Table S2 and S3).[27,56] The excellent stability of D-U-CoNi-OH electrode toward electrochemical OER in alkaline was demonstrated by CV cycling and

constant potential methods, respectively (Figure S23). Similar with the above methods, we also recorded the polarization plots of D-U-CoNi-OH in purified 1M KOH, unpurified 1M KOH, and 2 mM Fe + unpurified 1M KOH electrolytes, respectively, after their OER performances reach steady state. All plots were recorded without using *i*R-correction. As shown in Figure S24, the OER current in the unpurified electrolyte is higher than that in purified electrolyte and lower than that in the electrolyte of 2 mM Fe + unpurified 1M KOH, again proving the Fe impurities could have contributed to the high activity of D-U-CoNi-OH to some extent. To further demonstrate the versatility of this room-temperature synthesis method, the Co-MOF nanoarrays were successfully grown on different substrates, including carbon cloth paper (Figure S25), titanium mesh (Figure S26), and glass beaker wall (Figure S27).

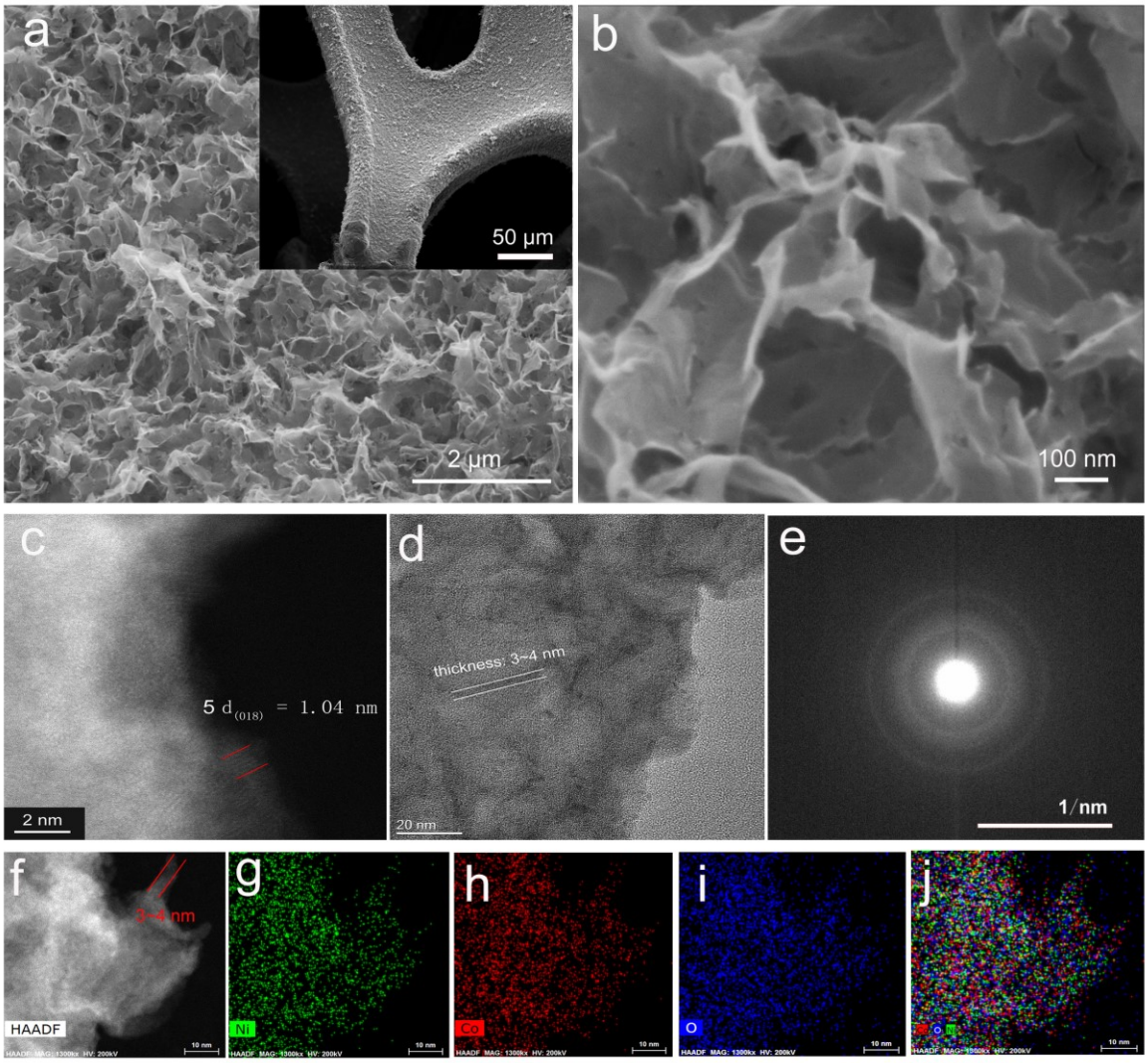

Figure 4. (a, b) SEM, (c) HAADF-STEM, (d) TEM, and (e) SAED images of Co-MOF nanoarray-derived ultrathin CoNi hydroxide nano-polycrystalline. (f-j) HAADF-STEM and elemental mapping images. The thickness measurement is shown in Figure d and f.

In summary, we demonstrated a simple, scalable, and efficient two-step strategy to synthesize grain-boundary rich ultrathin transition metal hydroxide nanosheet-networks on the conductive substrate at room temperature. We initially grow the Co-MOF (ZIF-L-Co) nanosheet arrays on Ni foam and then convert it into inorganic Co-M (M = Co and Ni) hydroxides through a facile etching process. The resulting nano-polycrystalline ultrathin TMHs exhibit superior activities toward OER in alkaline media. This two-step process offers a simple and scalable synthetic route towards defect-rich hierarchical nanostructures with tunable chemical compositions on versatile substrates. This synthetic route opens new opportunities in water splitting, metal-air batteries, fuel cells, carbon dioxide reduction, etc.

ASSOCIATED CONTENT

Supporting Information.

Additional photographs, material characterizations, electrochemical tests, and tables are presented in the supporting information, including photographs of electrodes, images of FESEM and HR-HAADF-STEM, TEM, XPS spectra, crystal information, Nyquist plots and Tafel slopes, activity comparison tables.

AUTHOR INFORMATION

Corresponding Author

*E-mail: shanhu@iastate.edu

Notes

The authors declare no financial conflict.

ACKNOWLEDGMENT

This material is based upon the work supported by the U.S. National Science Foundation (Grant No. CMMI-1663509). B.Z. was supported by the Catron Fellowship, College of Engineering, Iowa State University. We thank Prof. Hailiang Wang at Yale University for the helps on part of the materials synthesis and characterizations (XRD and XPS), and mechanism analysis.

REFERENCES

(1) Fu, Q.; Wu, T.; Fu, G.; Gao, T.; Han, J.; Yao, T.; Zhang, Y.; Zhong, W.; Wang, X.; Song, B. Skutterudite-Type Ternary $Co_{1-x}Ni_xP_3$ Nanoneedle Array Electrocatalysts for Enhanced Hydrogen and Oxygen Evolution. *ACS Energy Lett.* **2018**, *3*, 1744–1752.

(2) Zhang, B.; Lui, Y. H.; Ni, H.; Hu, S. Bimetallic $(Fe_xNi_{1-x})_2P$ Nanoarrays as Exceptionally Efficient Electrocatalysts for Oxygen Evolution in Alkaline and Neutral Media. *Nano Energy* **2017**, *38*, 553–560.

(3) Stamenkovic, V. R.; Strmcnik, D.; Lopes, P. P.; Markovic, N. M. Energy and Fuels from Electrochemical Interfaces. *Nat. Mater.* **2016**, *16*, 57–69.

(4) Li, Y.; Lu, J. Metal-Air Batteries: Will They Be the Future Electrochemical Energy Storage Device of Choice? *ACS Energy Lett.* **2017**, *2*, 1370–1377.

(5) Jin, H.; Guo, C.; Liu, X.; Liu, J.; Vasileff, A.; Jiao, Y.; Zheng, Y.; Qiao, S.-Z. Emerging Two-Dimensional Nanomaterials for Electrocatalysis. *Chem. Rev.* **2018**, *118*, 6337–6408.

(6) Zhang, H. Ultrathin Two-Dimensional Nanomaterials. *ACS Nano* **2015**, *9*, 9451–9469.

(7) Song, F.; Hu, X. Exfoliation of Layered Double Hydroxides for Enhanced Oxygen Evolution Catalysis. *Nat. Commun.* **2014**, *5*, 1–9.

(8) Wang, H.; Lee, H. W.; Deng, Y.; Lu, Z.; Hsu, P. C.; Liu, Y.; Lin, D.; Cui, Y. Bifunctional Non-Noble Metal Oxide Nanoparticle Electrocatalysts through Lithium-Induced Conversion for Overall Water Splitting. *Nat. Commun.* **2015**, *6*, 7261.

(9) Jiang, K.; Wang, H.; Cai, W. Bin; Wang, H. Li Electrochemical Tuning of Metal Oxide for Highly Selective CO_2 Reduction. *ACS Nano* **2017**, *11*, 6451–6458.

(10) Yu, J.; Wang, Q.; O'Hare, D.; Sun, L. Preparation of Two Dimensional Layered Double Hydroxide Nanosheets and Their Applications. *Chem. Soc. Rev.* **2017**, *46*, 5950–5974.

(11) Zhang, B.; Hu, S. Turning Ni-Based Hydroxide into an Efficient Hydrogen Evolution Electrocatalyst by Fluoride Incorporation. *Electrochem. Commun.* **2018**, *86* , 108–112.

(12) Ma, R.; Sasaki, T. Two-Dimensional Oxide and Hydroxide Nanosheets: Controllable High-Quality Exfoliation, Molecular Assembly, and Exploration of Functionality. *Acc. Chem. Res.* **2015**, *48*, 136–143.

(13) Liang, H.; Meng, F.; Cabán-Acevedo, M.; Li, L.; Forticaux, A.; Xiu, L.; Wang, Z.; Jin, S. Hydrothermal Continuous Flow Synthesis and Exfoliation of NiCo Layered Double Hydroxide Nanosheets for Enhanced Oxygen Evolution Catalysis. *Nano Lett.* **2015**, *15*, 1421–1427.

(14) Wang, H.; Lu, Z.; Xu, S.; Kong, D.; Cha, J. J.; Zheng, G.; Hsu, P.-C.; Yan, K.; Bradshaw, D.; Prinz, F. B.; et al. Electrochemical Tuning of Vertically Aligned MoS_2 Nanofilms and Its Application in Improving Hydrogen Evolution Reaction. *Proc. Natl. Acad. Sci.* **2013**, *110*, 19701–19706.

(15) Zheng, Y.; Qiao, S.-Z. Metal-Organic Framework Assisted Synthesis of Single-Atom Catalysts for Energy Applications. *Natl. Sci. Rev.* **2018**, No. June, 1–2.

(16) Cai, G.; Zhang, W.; Jiao, L.; Yu, S. H.; Jiang, H. L. Template-Directed Growth of Well-Aligned MOF Arrays and Derived Self-Supporting Electrodes for Water Splitting. *Chem* **2017**, *2*, 791–802.

(17) Ma, T. Y.; Dai, S.; Jaroniec, M.; Qiao, S. Z. Metal-Organic Framework Derived Hybrid Co_3O_4-Carbon Porous Nanowire Arrays as Reversible Oxygen Evolution Electrodes. *J. Am. Chem. Soc.* **2014**, *136*, 13925–13931.

(18) Zhou, J.; Dou, Y.; Zhou, A.; Shu, L.; Chen, Y.; Li, J. R. Layered Metal-Organic Framework-Derived Metal Oxide/Carbon Nanosheet Arrays for Catalyzing the Oxygen Evolution Reaction. *ACS Energy Lett.* **2018**, *3*, 1655–1661.

(19) Zhang, J.; Li, Z.; Chen, Y.; Gao, S.; Lou, X. W. (David). Nickel–Iron Layered Double Hydroxide Hollow Polyhedrons as a Superior Sulfur Host for Lithium–Sulfur Batteries. *Angew. Chemie - Int. Ed.* **2018**, *57*, 10944–10948.

(20) Deshmukh, R.; Mehra, A.; Thaokar, R. Formation and Shape-Control of Hierarchical Cobalt Nanostructures Using Quaternary Ammonium Salts in Aqueous Media. *Beilstein J. Nanotechnol.* **2017**, *8*, 494–505.

(21) Zhang, J.; Zhang, T.; Yu, D.; Xiao, K.; Hong, Y. Transition from ZIF-L-Co to ZIF-67: A New Insight into the Structural Evolution of Zeolitic Imidazolate Frameworks (ZIFs) in Aqueous Systems. *CrystEngComm* **2015**, *17*, 8212–8215.

(22) Wang, H.; Robinson, J. T.; Diankov, G.; Dai, H. Nanocrystal Growth on Graphene with Various Degrees of Oxidation. *J. Am. Chem. Soc.* **2010**, *132*, 3270–3271.

(23) Gayer, K. H.; Woontner, L. Hydrolysis of Cobalt Chloride and Nickel Chloride at 25°. *J. Am. Chem. Soc.* **1952**, *74*, 1436–1437.

(24) Favaro, M.; Yang, J.; Nappini, S.; Magnano, E.; Toma, F. M.; Crumlin, E. J.; Yano, J.; Sharp, I. D. Understanding the Oxygen Evolution Reaction Mechanism on CoO_x Using *Operando* Ambient-Pressure X-Ray Photoelectron Spectroscopy. *J. Am. Chem. Soc.* **2017**, *139*, 8960–8970.

(25) Wu, D.; Wei, Y.; Ren, X.; Ji, X.; Liu, Y.; Guo, X.; Liu, Z.; Asiri, A. M.; Wei, Q.; Sun, X. $Co(OH)_2$ Nanoparticle-Encapsulating Conductive Nanowires Array: Room-Temperature Electrochemical Preparation for High-Performance Water Oxidation Electrocatalysis. *Adv. Mater.* **2018**, *30*, 1–7.

(26) Zhang, B.; Jiang, K.; Wang, H.; Hu, S. Fluoride-Induced Dynamic Surface Self-Reconstruction Produces Unexpectedly Efficient Oxygen Evolution Catalyst. *Nano Lett.* **2018**, acs.nanolett.8b04466.

(27) Zhang, B.; Zheng, X.; Voznyy, O.; Comin, R.; Bajdich, M.; Arquer, F. P. G. De; Dinh, C. T.; Fan, F.; Yuan, M.; Janmohamed, A.; et al. Homogeneously Dispersed, Multimetal Oxygen-Evolving Catalysts. *Science* **2016**, *352*, 333–338.

(28) Ping, J.; Wang, Y.; Lu, Q.; Chen, B.; Chen, J.; Huang, Y.; Ma, Q.; Tan, C.; Yang, J.; Cao, X.; et al. Self-Assembly of Single-Layer CoAl-Layered Double Hydroxide Nanosheets on 3D Graphene Network Used as Highly Efficient Electrocatalyst for Oxygen Evolution

Reaction. *Adv. Mater.* **2016**, *28*, 7640–7645.

(29) Jin, H.; Wang, J.; Su, D.; Wei, Z.; Pang, Z.; Wang, Y. In Situ Cobalt-Cobalt Oxide/N-Doped Carbon Hybrids as Superior Bifunctional Electrocatalysts for Hydrogen and Oxygen Evolution. *J. Am. Chem. Soc.* **2015**, *137*, 2688–2694.

(30) Wang, Y.; Zhang, Y.; Liu, Z.; Xie, C.; Feng, S.; Liu, D.; Shao, M.; Wang, S. Layered Double Hydroxide Nanosheets with Multiple Vacancies Obtained by Dry Exfoliation as Highly Efficient Oxygen Evolution Electrocatalysts. *Angew. Chemie - Int. Ed.* **2017**, *56*, 5867–5871.

(31) Guo, P.; Wu, J.; Li, X. B.; Luo, J.; Lau, W. M.; Liu, H.; Sun, X. L.; Liu, L. M. A Highly Stable Bifunctional Catalyst Based on 3D $Co(OH)_2$@NCNTs@NF Towards Overall Water-Splitting. *Nano Energy* **2018**, *47*, 96–104.

(32) Zhang, Y.; Shao, Q.; Long, S.; Huang, X. Cobalt-Molybdenum Nanosheet Arrays as Highly Efficient and Stable Earth-Abundant Electrocatalysts for Overall Water Splitting. *Nano Energy* **2018**, *45*, 448–455.

(33) Song, F.; Hu, X. Ultrathin Cobalt-Manganese Layered Double Hydroxide Is an Efficient Oxygen Evolution Catalyst. *J. Am. Chem. Soc.* **2014**, *136*, 16481–16484.

(34) McAteer, D.; Godwin, I. J.; Ling, Z.; Harvey, A.; He, L.; Boland, C. S.; Vega-Mayoral, V.; Szydłowska, B.; Rovetta, A. A.; Backes, C.; et al. Liquid Exfoliated $Co(OH)_2$ Nanosheets as Low-Cost, Yet High-Performance, Catalysts for the Oxygen Evolution Reaction. *Adv. Energy Mater.* **2018**, 1702965.

(35) Liang, Y.; Li, Y.; Wang, H.; Zhou, J.; Wang, J.; Regier, T.; Dai, H. Co_3O_4 Nanocrystals on Graphene as a Synergistic Catalyst for Oxygen Reduction Reaction. *Nat. Mater.* **2011**, *10*, 780–786.

(36) Mao, S.; Wen, Z.; Huang, T.; Hou, Y.; Chen, J. High-Performance Bi-Functional Electrocatalysts of 3D Crumpled Graphene-Cobalt Oxide Nanohybrids for Oxygen Reduction and Evolution Reactions. *Energy Environ. Sci.* **2014**, *7*, 609–616.

(37) Huang, L.; Jiang, J.; Ai, L. Interlayer Expansion of Layered Cobalt Hydroxide Nanobelts to Highly Improve Oxygen Evolution Electrocatalysis. *ACS Appl. Mater. Interfaces* **2017**, *9*, 7059–7067.

(38) Kim, J. E.; Lim, J.; Lee, G. Y.; Choi, S. H.; Maiti, U. N.; Lee, W. J.; Lee, H. J.; Kim, S. O. Subnanometer Cobalt-Hydroxide-Anchored N-Doped Carbon Nanotube Forest for Bifunctional Oxygen Catalyst. *ACS Appl. Mater. Interfaces* **2016**, *8*, 1571–1577.

(39) Nai, J.; Yin, H.; You, T.; Zheng, L.; Zhang, J.; Wang, P.; Jin, Z.; Tian, Y.; Liu, J.; Tang, Z.; et al. Efficient Electrocatalytic Water Oxidation by Using Amorphous Ni-Co Double Hydroxides Nanocages. *Adv. Energy Mater.* **2015**, *5*, 1–7.

(40) Liu, P. F.; Yang, S.; Zheng, L. R.; Zhang, B.; Yang, H. G. Electrochemical Etching of α-Cobalt Hydroxide for Improvement of Oxygen Evolution Reaction. *J. Mater. Chem. A* **2016**, *4*, 9578–9584.

(41) Han, X.; Yu, C.; Yang, J.; Zhao, C.; Huang, H.; Liu, Z.; Ajayan, P. M.; Qiu, J. Mass and Charge Transfer Coenhanced Oxygen Evolution Behaviors in CoFe-Layered Double Hydroxide Assembled on Graphene. *Adv. Mater. Interfaces* **2016**, *3*, 1–8.

(42) Kim, H.; Kim, Y.; Noh, Y.; Kim, W. B. Ultrathin Amorphous α-$Co(OH)_2$ nanosheets Grown on Ag Nanowire Surfaces as a Highly Active and Durable Electrocatalyst for Oxygen Evolution Reaction. *Dalt. Trans.* **2016**, *45*, 13686–13690.

(43) Qi, Z.; Xiao, C.; Liu, C.; Goh, T. W.; Zhou, L.; Maligal-Ganesh, R.; Pei, Y.; Li, X.; Curtiss, L. A.; Huang, W. Sub-4 nm PtZn Intermetallic Nanoparticles for Enhanced Mass and Specific Activities in Catalytic Electrooxidation Reaction. *J. Am. Chem. Soc.* **2017**, *139*, 4762–4768.

(44) Stevens, M. B.; Enman, L. J.; Batchellor, A. S.; Cosby, M. R.; Vise, A. E.; Trang, C. D. M.; Boettcher, S. W. Measurement Techniques for the Study of Thin Film Heterogeneous Water Oxidation Electrocatalysts. *Chem. Mater.* **2017**, *29*, 120–140.

(45) Seitz, L. C.; Dickens, C. F.; Nishio, K.; Hikita, Y.; Montoya, J.; Doyle, A.; Kirk, C.; Vojvodic, A.; Hwang, H. Y.; Norskov, J. K.; et al. A Highly Active and Stable $IrO_x/SrIrO_3$ Catalyst for the Oxygen Evolution Reaction. *Science* **2016**, *353*, 1011–1014.

(46) Suntivich, J.; May, K. J.; Gasteiger, H. A.; Goodenough, J. B.; Shao-Horn, Y. A Perovskite Oxide Optimized for Molecular Orbital Principles. *Science* **2011**, *334*, 2010–2012.

(47) Zhang, B.; Lui, Y. H.; Zhou, L.; Tang, X.; Hu, S. An Alkaline Electro-Activated Fe–Ni Phosphide Nanoparticle-Stack Array for High-Performance Oxygen Evolution under Alkaline and Neutral Conditions. *J. Mater. Chem. A* **2017**, *5*, 13329–13335.

(48) Li, C.; Han, X.; Cheng, F.; Hu, Y.; Chen, C.; Chen, J. Phase and Composition Controllable Synthesis of Cobalt Manganese Spinel Nanoparticles towards Efficient

Oxygen Electrocatalysis. *Nat. Commun.* **2015**, *6*, 1–8.

(49) Paoli, E. A.; Masini, F.; Frydendal, R.; Deiana, D.; Schlaup, C.; Malizia, M.; Hansen, T. W.; Horch, S.; Stephens, I. E. L.; Chorkendorff, I. Oxygen Evolution on Well-Characterized Mass-Selected Ru and RuO_2 Nanoparticles. *Chem. Sci.* **2015**, *6*, 190–196.

(50) Wu, L.; Li, Q.; Wu, C. H.; Zhu, H.; Mendoza-Garcia, A.; Shen, B.; Guo, J.; Sun, S. Stable Cobalt Nanoparticles and Their Monolayer Array as an Efficient Electrocatalyst for Oxygen Evolution Reaction. *J. Am. Chem. Soc.* **2015**, *137*, 7071–7074.

(51) Trotochaud, L.; Young, S. L.; Ranney, J. K.; Boettcher, S. W. Nickel-Iron Oxyhydroxide Oxygen-Evolution Electrocatalysts : The Role of Intentional and Incidental Iron Incorporation. *J. Am. Chem. Soc* **2014**, *136*, 6744–6753.

(52) Burke, M. S.; Kast, M. G.; Trotochaud, L.; Smith, A. M.; Boettcher, S. W. Cobalt-Iron (Oxy)Hydroxide Oxygen Evolution Electrocatalysts: The Role of Structure and Composition on Activity, Stability, and Mechanism. *J. Am. Chem. Soc.* **2015**, *137*, 3638–3648.

(53) Han, L.; Dong, S.; Wang, E. Transition-Metal (Co, Ni, and Fe)-Based Electrocatalysts for the Water Oxidation Reaction. *Adv. Mater.* **2016**, *28*, 9266–9291.

(54) Song, Z.; Han, X.; Deng, Y.; Zhao, N.; Hu, W.; Zhong, C. Clarifying the Controversial Catalytic Performance of $Co(OH)_2$ and Co_3O_4 for Oxygen Reduction/Evolution Reactions toward Efficient Zn-Air Batteries. *ACS Appl. Mater. Interfaces* **2017**, *9*, 22694–22703.

(55) Yu, J.; Li, Q.; Li, Y.; Xu, C. Y.; Zhen, L.; Dravid, V. P.; Wu, J. Ternary Metal Phosphide

with Triple-Layered Structure as a Low-Cost and Efficient Electrocatalyst for Bifunctional Water Splitting. *Adv. Funct. Mater.* **2016**, *26*, 7644–7651.

(56) Huang, J.; Han, J.; Wang, R.; Zhang, Y.; Wang, X.; Zhang, X.; Zhang, Z.; Zhang, Y.; Song, B.; Jin, S. Improving Electrocatalysts for Oxygen Evolution Using $Ni_xFe_{3-x}O_4$/Ni Hybrid Nanostructures Formed by Solvothermal Synthesis. *ACS Energy Lett.* **2018**, *3*, 1698–1707.